npj Computational Materials

www.nature.com/npjcompumats

ARTICLE OPEN

Check for updates

Role of atomic-scale thermal fluctuations in the coercivity

Yuta Toga[1,2,3]✉, Seiji Miyashita[2,3,4], Akimasa Sakuma[5] and Takashi Miyake[2,6]

The microscopic mechanism of coercivity at finite temperature is a crucial issue for permanent magnets. Here we present the temperature dependence of the coercivity of an atomistic spin model for the highest-performance magnet $Nd_2Fe_{14}B$. For quantitative analysis of the magnetization reversal with thermal fluctuations, we focus on the free energy landscape as a function of the magnetization. The free energy is calculated by the replica-exchange Wang–Landau method. This approach allows us to address a slow nucleation problem, i.e., thermal activation effects, in the magnetization reversal. We concretely observed that the thermal fluctuations lead to a downward convexity in the coercivity concerning the temperature. Additionally, through analyzing the microscopic process of the thermal activation (nucleation), we discover the activation volume is insensitive to a magnetic field around the coercivity. The insensitivity explains the linear reduction of the free energy barrier by the magnetic field in the nucleation process.

npj Computational Materials (2020)6:67 ; https://doi.org/10.1038/s41524-020-0325-6

INTRODUCTION

Demands on high-performance permanent magnets have become an imperative subject of the save-energy technology for sustainable environments[1,2]. To improve the performance of magnets, there is often a great desire to understand the temperature dependence of coercivity. Experimental and theoretical researches have been extensively carried out to investigate the microscopic understanding of the coercivity mechanism from atomic-scale magnetic structure[3–10]. Recently, a scanning hard X-ray microprobe was employed to visualize the nucleation and domain wall motion of magnetization reversal processes from the grain boundary interfaces in the highest performance magnet $Nd_2Fe_{14}B$[8]. Until now, a study on the microscopic approach to temperature effects on coercivity, especially a slow nucleation process, has not been reported. The nucleation leads to the observation time dependence of the coercivity. This is phenomenologically known as coercivity reduction by thermal activation effect[11–15].

Large reduction of coercivity from the theoretically expected value is an essential current problem which has been called "Discrepancy to theory" by Kronmüller et al.[16]. In this regard, extensive works have been done to elucidate the reason for the discrepancy[17–21], but not yet clear from the atomistic viewpoint. The present paper studies the reduction due to thermal fluctuations. The magnetization reversal is a transition from a metastable state to a stable state by overcoming energy barriers under a reverse magnetic field. In this overcoming process, a reverse nucleus is formed. Under thermal fluctuations, the nucleation occurs stochastically, that is, thermal-activated relaxation. Thus the coercivity, i.e., the threshold field, depends on the observation time. In the permanent magnet applications, the metastable state is required to be stable for the duration of the order of a second. To handle such a slow relaxation process, a method that uses the energy landscape has been developed, also known as the minimum energy path (MEP)[22]. For the magnetization reversal, MEP has been studied in the continuum approximation models with parameters with respect to a given temperature[15,18,19,23]. However, the aforementioned method has not considered thermal fluctuations. In the present work, we propose an approach to evaluate the temperature dependence of the coercivity from a microscopic viewpoint by using an atomistic model. In contrast to the MEP, the present technique directly handles thermal fluctuations and also the atomistic information in the magnetization reversal process. In particular, we focus on the Neodymium (Nd) magnet $Nd_2Fe_{14}B$[24].

The coercivity is a non-equilibrium concept concerning the collapse of a metastable state, but not expressed by an equilibrium expectation value. Thus, we need a dynamical model. The relaxation time is estimated from the free-energy barrier F_B by using the form (like Arrhenius law):

$$\tau = \tau_0 e^{\beta F_B}, \tag{1}$$

where τ_0 is the reciprocal of the attempt frequency, which is typically set to 10^{-11} s[12]. Then, for the observation time of 1 s, setting $\tau = 1$ s, the barrier height is given by $F_B = 25.3\, k_B T$. The free energy is given by the $Nd_2Fe_{14}B$ atomistic spin Hamiltonian, which was recently developed and successfully reproduced static properties of the $Nd_2Fe_{14}B$ magnet (shown in "Methods")[25].

To calculate the free energy as a function of the z-component of the magnetization $F(M_z)$ for a huge system (up to 24.6 nm × 24.6 nm × 25.6 nm, 1,130,626 spins), the size required to handle a nucleation process, we have developed an approach for the coercivity calculation based on the replica-exchange Wang–Landau (REWL) method[26,27]. Remarkably, we can perform an efficient parallelization scheme for the original Wang–Landau Monte Carlo (WLMC) method[28] (see "Methods").

RESULTS AND DISCUSSION

Temperature dependence of the coercivity

The obtained $F(M_z)$ for zero magnetic field ($H_z = 0$) at $T = 0.46\, T_C^{cal}$ is depicted in Fig. 1a by the red curve (T_C^{cal} is the Curie temperature of the model). Notably, this is the quantitatively correct (not schematic) form of $F(M_z)$ for an atomistic spin model

[1]National Institute for Materials Science (NIMS), Tsukuba 305-0047, Japan. [2]Elements Strategy Initiative Center for Magnetic Materials (ESICMM), Tsukuba, Japan. [3]Institute for Solid State Physics, University of Tokyo, Kashiwa 277-8581, Japan. [4]The Physical Society of Japan, Tokyo 113-0033, Japan. [5]Department of Applied Physics, Tohoku University, Sendai 980-8579, Japan. [6]National Institute of Advanced Industrial Science and Technology (AIST), Tsukuba 305-8568, Japan. ✉email: toga@issp.u-tokyo.ac.jp

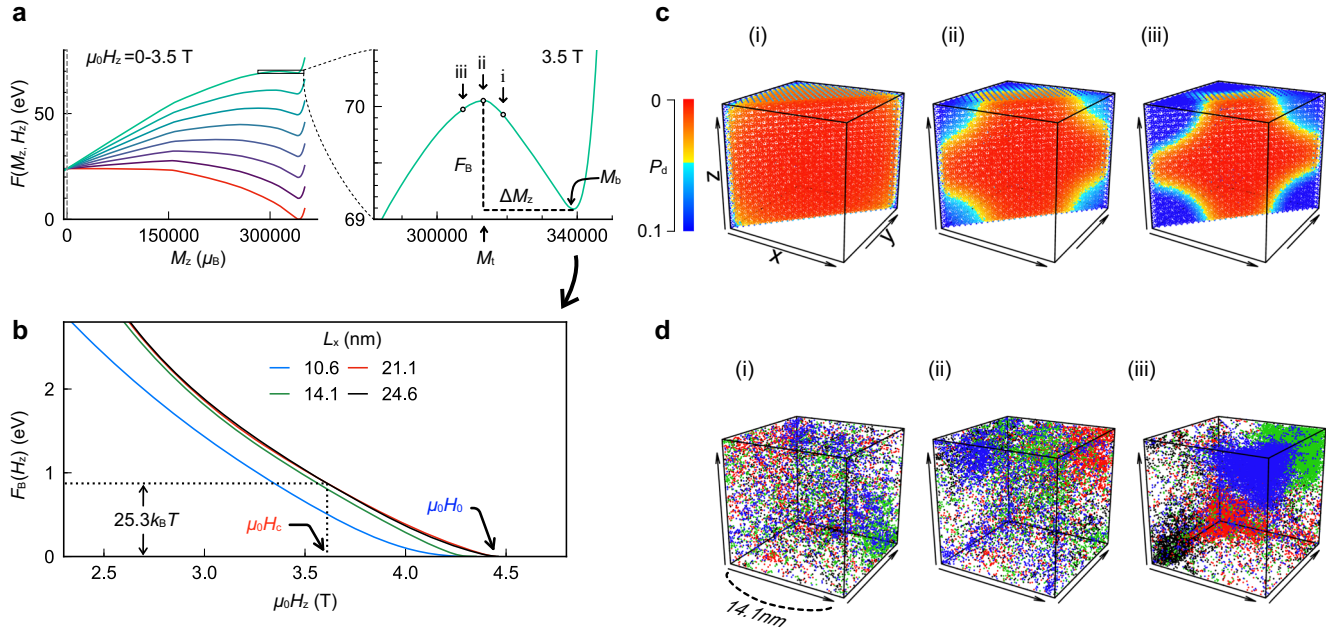

Fig. 1 Free energy landscape simulation. a Free energies as a function of M_z for the $Nd_2Fe_{14}B$ isolated grains at 0.46 T_C^{cal}, whose size is (L_x, L_y, L_z) = (14.1, 14.1, 14.6) nm (212,536 spins). Red line is for $H_z = 0$ and other lines are for applying H_z. **b** Free-energy barriers as a function of $\mu_0 H_z$ for four system sizes: L_x = 10.6, 14.1, 21.1, and 24.6 nm ($L_y = L_x$, $L_z = 1.038L_x$), evaluated from $F(M_z, H_z)$ similar to Fig. 1a. **c** The distributions of reversed probability P_d at Fe spins sliced by (110) plane, which correspond to the points (i–iii) in Fig. 1a. **d** Four MC snapshots of reversed Fe spins for the three points.

representing the $Nd_2Fe_{14}B$ magnet. Shapes of the free energy with the reverse magnetic fields H_z are exactly given by $F(M_z) + \mu_0 H_z M_z$. This is clearly illustrated in Fig. 1a. Close to the spinodal point, the point at which the metastability disappears, magnetization reversal occurs when the free energy barrier F_B (see Fig. 1a) becomes compatible with the temperature. The H_z dependence of F_B is given in Fig. 1b, where we define H_0 as the field at which $F_B = 0$. Similarly, H_c is defined as the field at which $F_B = 25.3\ k_BT$. We call the former "spinodal field" and the latter "coercivity with thermal activation". As mentioned above, H_c corresponds to the coercive field for the observation time $\tau = 1.0$ s. In order to see how the magnetization reversal initiates, in Fig. 1c, we depict the spatial distributions of the magnetization reversal probability at the points shown by arrows in Fig. 1a, which were obtained by the REWL method. As expected, we found out that the reversal begins at the corner. There are two reasons for this reversal: One is the decrease of a local magnetic anisotropy due to surface thermal fluctuations. Secondly, the reduction of an exchange energy by decouplings at the corner facilitates the nucleation. Here, all the corners are equivalent, and symmetric configurations are found. However, in an individual process, one of the corners is selected. Figure 1d illustrates a plot of MC snapshots at the corresponding fields.

The temperature dependencies of several formulae for the coercivities are depicted in Fig. 2, and are compared with the ideal coercivity H_k. Here, we determined H_k as H_0 of the same system size with the periodic boundary condition. In the calculated temperature range, we confirmed that H_k takes almost same value as the magnetic anisotropy field $H_a = 2K_1/\mathcal{M}_s$, where K_1 is the magnetic anisotropy constant[20,25] and $\mathcal{M}_s$ is the saturated magnetization at the given temperature. The coercivity H_r of permanent magnets is reduced from its limit value H_k by various external influences. These reductions have been expressed in the following forms[13,16]:

$$\begin{aligned} H_r &= \alpha H_k - H_t - \mathcal{M}_s N_d \\ &= \alpha' H_k - \mathcal{M}_s N_d, \end{aligned} \tag{2}$$

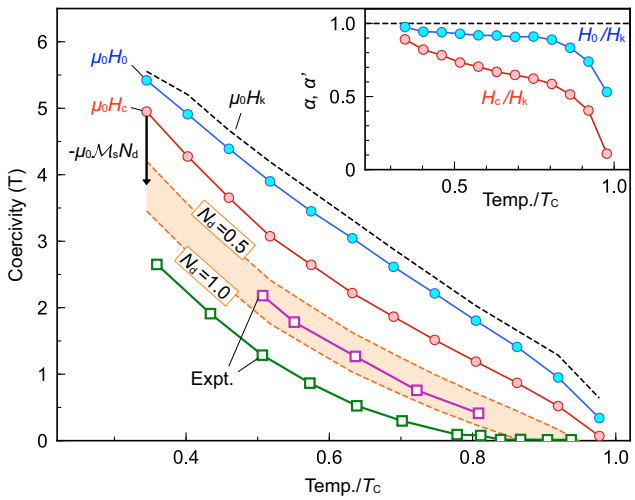

Fig. 2 Temperature dependence of coercivity. The blue line $\mu_0 H_0$ and the red line $\mu_0 H_c$ were calculated from Fig. 1b for 21.1 nm × 21.1 nm × 21.9 nm (713,172 spins) isolated grain at each temperature. The colored area depicts the coercivity $\mu_0 H_c$ under the demagnetization fields in the range of demagnetization factor N_d = 0.5–1.0. The green and purple squared lines denote the experimental measurements in sintered[29] and the hot-deformed with grain boundary diffusion of Nd-Cu alloy[14] magnets, respectively. Inset shows $\alpha = H_0/H_k$ and $\alpha' = H_c/H_k$.

where $H_t = H_0 - H_c$ and $\alpha = H_0/H_k$. Here, H_t and α represent the thermal activation field and phenomenological factor, respectively. The factor α often means the reduction due to the microstructure such as defects, and the surfaces. On the other hand, $\alpha' = H_c/H_k$ is an expression with an alternate definition for H_k including H_t. The second line of Eq. 2 is known as "Kronmüller equation". The terms of the demagnetization field $-\mathcal{M}_s N_d$ express the reduction due to the dipole–dipole (DD) interaction.

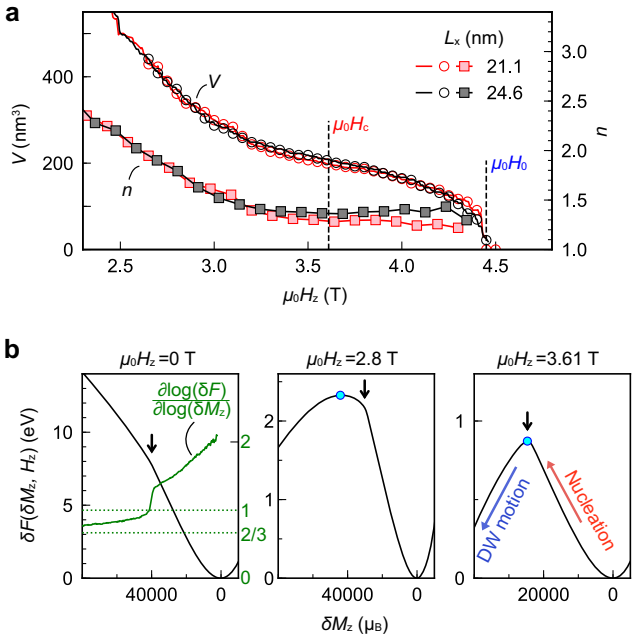

Fig. 3 Magnetic field dependence of activation volume. a The activation volume V as a function of $\mu_0 H_z$ for two system sizes at $0.46\,T_C^{cal}$. Circle points are evaluated from Eq. 3 while solid lines are evaluated from Eq. 4. Squared lines are the exponent n of free energy barrier in formula 6. **b** Field dependence of the shape of free energy as a function of δM_z for $L_x = 24.6$ nm. Blue points are the top of the free energy barrier, which corresponds to M_t, and black arrows denote the cusp in the free energy. Green line shows the value on the right axis.

Our approach can handle the temperature dependence of α and H_t explicitly. Unlike the continuum approximation, temperature is naturally introduced in our model by the Boltzmann weights in the MC simulation. This is because we used the atomistic model. The continuum approximation works with temperature-dependent input parameters in which thermal fluctuations are not included in the motion. We have also plotted the results of coercivity H_r with respect to the demagnetization factors $N_d = 0.5$ and 1.0 with temperature-dependent magnetization $\mathcal{M}_s$. Since the demagnetization field $-N_d\mathcal{M}_s$ approximately introduces the effects of the DD interaction as the uniform field, so it cannot consider the size and shape dependences of N_d[30]. However, the simulation results qualitatively validate those of the experiments because an increase in temperature leads to a downward convexity in coercivity even without $-N_d\mathcal{M}_s$. The effects of the DD interaction will be discussed later. In the figure, we compare the result with experimental observations. The green squares are data for a sintered sample and the purple ones for a diffused hot-deformed sample. In the former, the effect of polycrystalline causes a further reduction[31], while in the latter grains are separated and compatible with the present calculation. In the former case, other effects would subject to the multi-grain approach in the future. Thus, the present result gives the upper limit of the coercivity at finite temperatures.

For some sintered polycrystalline magnets (corresponding to the green line in Fig. 2), Kronmüller and Durst phenomenologically estimated the decay factor as $\alpha'_{exp} = 0.89 - 0.93$ from measured magnetic properties around room temperature[16]. In the inset of Fig. 2, we show the temperature dependence of α and α'. The difference of α from 1 reflects the decrease of the surface magnetic anisotropy by thermal fluctuations, and α' also includes the thermal activation effects. The decay factors at room temperature (here, $T = 0.51\,T_C$) are determined as $\alpha = 0.93$ and $\alpha' = 0.73$. In the case of the experiment, exchange interactions at the grain boundary interfaces suppress the interface thermal fluctuations. The suppression is one of the origins of the difference between α'_{exp} and α'.

Nucleation mechanism

Next, we consider the mechanism of the thermal activation (nucleation) process for which the concept of "activation volume" has been introduced[11–15]. The symbol ΔM_z represents the difference of the magnetization between those at the local minimum $M_z = M_b$ of the free energy and those at the local maximum $M_z = M_t$ (see Fig. 1a). It is confirmed that ΔM_z gives the activation volume V:

$$V = \Delta M_z/\mathcal{M}_s. \tag{3}$$

Note that the unit of $\mathcal{M}_s$ is (μ_B/volume). Activation volume has been defined by

$$V = -\frac{1}{\mu_0\mathcal{M}_s}\frac{\partial F_B}{\partial H_z}. \tag{4}$$

By differentiating F_B:

$$\begin{aligned} F_B(H_z) &= F(M_t, H_z) - F(M_b, H_z) \\ &= F(M_t, 0) - F(M_b, 0) + \mu_0 H_z(M_t - M_b), \end{aligned} \tag{5}$$

it is obvious that definition Eqs. 3 and 4 are equivalent. Here, we note that $F(M_{t(b)}, 0)$ depends on H_z since $M_{t(b)}$ is a function of H_z. In Fig. 3a, the activation volumes obtained by the both definitions Eqs. 3 and 4 were plotted. This confirms the equivalence.

From Eq. 4, the field dependence of F_B is related to the nucleation process. Thus, we focus on the exponent n which is widely used for the dependence in the phenomenological form:

$$F_B \propto (1 - H_z/H_0)^n. \tag{6}$$

The exponent n is 2 for coherent magnetization reversal. However, according to the authors[12,14], the experimental value for n was given to be approximately 1.0. We evaluated the value of n in the atomistic magnetization reversal process around the coercivity. It should be noted that the value of n varies depending on the range of $\mu_0 H_z$ (shown in Fig. 3a), where we fit the data. However, for a wide range of $\mu_0 H_z$, it was observed that the value of n was approximately 1.3. We, therefore, propose that the small value of n is ascribed to the peculiar shape of the free energy. Here we define $\delta F(\delta M_z)$ for the free energy near the local minimum, i.e., $\delta F(\delta M_z) = F(M_b - \delta M_z) - F(M_b)$, where $\delta F(\Delta M_z) = F_B$. The shapes of $\delta F(\delta M_z)$ for the fields $\mu_0 H_z = 0$, 2.8, and 3.61 T are depicted in Fig. 3b, where a cusp is pointed by the arrow in each figure.

The cusp represents the point at which the type of the magnetization reversal changes[32]: for small value of δM_z (see in Fig. 3b), the reversal process is the nucleation type, where we expect

$$\delta F(\delta M_z) \propto \delta M_z, \tag{7}$$

while for large value of δM_z, $\delta F(\delta M_z)$ is mainly given by the change due to a domain wall (DW) motion, where we expect

$$\delta F(\delta M_z) \propto \delta M_z^{2/3} + \text{const.} \tag{8}$$

This magnetization reversal mechanism is schematically pictured in Fig. 4. This difference can be understood in the following picture. In the case of the Heisenberg type with uniaxial anisotropy (corresponding to the $Nd_2Fe_{14}B$ spin model), the critical nucleation size ($\Delta M_z^{1/3} \equiv R_c$) is about the domain wall width δ_{dw}. And thus, before the cusp point ($R < R_c$, where R is the width of the magnetization reversing region, see Fig. 4b) the nucleation region is growing where we have Eq. 7. Around the cusp point, a fully reversed region appears. And after this point, the excess free energy δF comes from the domain wall, i.e.,

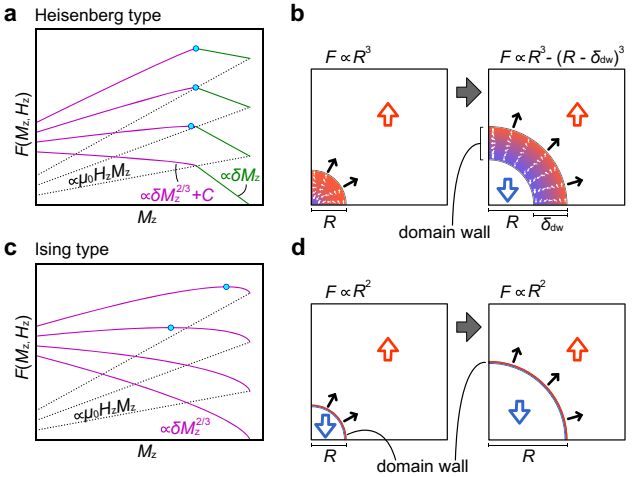

Fig. 4 Nucleation picture in permanent magnets. Schematic pictures of **a**, **c** energy landscape and **b**, **d** spin configuration in the magnetization reversal processes at low-temperature limit. **a**, **b** Heisenberg type spin model with uniaxial magnetic anisotropy. **c**, **d** Ising type. The energy landscapes under several magnetic fields are drawn (the lowest line is for $H_z = 0$). Dotted lines are the reverse magnetic field terms $\mu_0 H_z M_z$ and blue points are the top of the energy barriers.

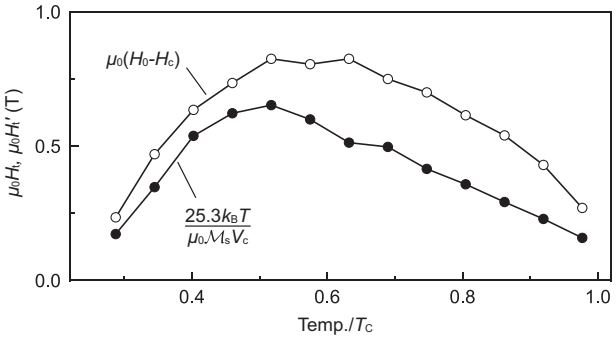

Fig. 5 Thermal activation reduction. The shifts of the coercivity due to the thermal activation effects, evaluated from the two ways: $H_t = H_0 - H_c$ and Eq. 10.

the surface of the fully reversed region. In this case we have Eq. 8. For comparison, we show the case of Ising model where δ_{dw} is much smaller than R_c at low temperatures, and we have the dependence Eq. 8 for almost all R except very small R. This comparison is schematically pictured in Fig. 4d.

To clearly see the change of exponent, in Fig. 3b, we show the differentiate $\log(\delta F)$ by $\log(\delta M_z)$ with the green curve which gives roughly the power k when we assume the dependence: $\delta F = C\delta M_z^k + D$ (C and D are constant). We find that k is close to 2/3 for large δM_z and jump at the cusp. Around $\delta M_z = 0$, thermal fluctuations enhance the behavior of $k = 2$, i.e.,

$$\delta F(\delta M_z) \propto \delta M_z^2, \tag{9}$$

which makes it difficult to identify the behavior $\delta F \propto \delta M_z$ (i.e., $k = 1$) for the nucleation process. This fact causes that we have an intermediate value ($n \simeq 1.3$) numerically. However, k clearly changes from 2 to 1 with δM_z, which supports the present scenario.

In any case, δF has regions of upward convex and downward convex between which the cusp exists. This structure causes ΔM_z to be less dependent on H_z for a range of H_z[33], which can be seen from comparing the blue points in Fig. 4a, c. In this range, V is a constant and it results in the value of $n = 1$ by Eq. 4. Note that, the reason for the cusp explains the drastic change in the magnetization distribution between (i) and (iii) in Fig. 1c, d.

If we assume $n = 1$ for any H_z, then the result is the widely used phenomenological equation for the thermal activation effects[13]:

$$H_t' = \frac{25.3 k_B T}{\mu_0 \mathcal{M}_s V_c}, \tag{10}$$

where V_c is the value of V at $H_z = H_c$. In Fig. 5, we compare the temperature dependence of H_t and H_t'. We found a qualitatively similar dependence. The difference between H_t' and H_t becomes significant in the high-temperature range, which is attributed to the fact that the activation volume and n are not exactly constant. Thus, the difference due to the changes in the magnetization reversal type and surface effects, as shown in Figs. 3 and 4.

It is necessary to mention the exact effects of the DD interaction, which is approximately introduced as the demagnetization field in the present study. The DD interaction brings the non-uniformity of local demagnetization fields near corners and edges in grains, unlike the demagnetization field. The non-uniformity should change the nucleation process from the calculation results. However, the strength of the local field increases logarithmically with system size[30,34,35], and the nucleation behavior is protected by the cusp structure. Thus, the nucleation mechanism we proposed is expected not to qualitatively change up to a certain large grain size ($L_x \simeq 1 - 10\,\mu$m). Above this size, since magnetic domain structures are formed[36], the DD interaction should be incorporated into the spin Hamiltonian.

In summary, our atomistic approach by the free energy landscape simulations revealed essential characteristics of the thermal activation effects for permanent magnets, i.e., the downward convexity in the coercivity concerning the temperature, the microscopic definition of the activation (nucleation) volume, and also the exponent $n = 1$ for the well-used energy barrier formula (6). The present study should be the first step to study the characterization of coercivity at finite temperatures from microscopic information, and the method will be extended to the cases complex of grains with the DD interaction in the future.

METHODS

Atomistic spin model

The atomistic classical spin Hamiltonian of $Nd_2Fe_{14}B$ magnet was recently proposed for the study of thermodynamic properties at finite temperatures by using Monte Carlo (MC) method[20,25,35,37] and stochastic Landau–Lifshitz–Gilbert equation[38]. It is given by

$$\mathcal{H} = -2\sum_{i<j} J_{ij}\boldsymbol{s}_i \cdot \boldsymbol{s}_j - \sum_{i\in Fe} D_i (s_i^z)^2 - \sum_{i\in Nd}\sum_{l=2,4,6} D_i^l (s_i^z)^l, \tag{11}$$

where J_{ij} is the exchange coupling constants between the i-th and j-th spins up to a cut-off range (in the present work 3.52 Å), and $\boldsymbol{s}_i$ is the normalized spin moment at the i-th site. The second and third terms are the magnetic anisotropy of Fe and Nd sites, respectively. The coefficients J_{ij}, D_i, D_i^l and magnetic moments are determined from ab-initio calculations and experimental data[25]. Note that Curie temperature of the model with given parameters is $T_C^{cal} = 870$ K, which is higher than the experimental observation ($T_C^{exp} \simeq 585$ K). This difference must be adjusted by fine-tuning of the parameters, but the qualitative properties are well reproduced[20,25].

Wang–Landau method for magnetization

The partition function of a spin system is generally described as follows:

$$Z = \sum_{\boldsymbol{R}} e^{-\beta H(\boldsymbol{R})} = \sum_E \sum_{M_z} g(E, M_z) e^{-\beta E}, \tag{12}$$

where $\beta = 1/k_B T$ is the inverse temperature, E is the internal energy of a spin configuration $\boldsymbol{R}$, M_z is the z-component of a total magnetization and g

(E, M_z) is the joint density of states. By using $g(E, M_z)$, the magnetization dependence of the free energy $F(\beta, M_z)$ and a partial partition function Z_{M_z} can be defined by following formula:

$$F(\beta, M_z) = -\beta^{-1} \ln Z_{M_z}, \tag{13}$$

$$Z_{M_z} = \sum_E g(E, M_z) e^{-\beta E}. \tag{14}$$

The Wang–Landau Monte Carlo (WLMC) method[28] allows us to calculate $g(E, M_z)$ in the basis of a relation: $h(E, M_z) = g(E, M_z)w(E, M_z)$, where $h(E, M_z)$ is the histogram of the spin states obtained by MC sampling with a weight $w(E, M_z)$. If a flat histogram (h is constant) can be obtained by arbitrarily adjusting $w(E, M_z)$ in a MC simulation, $g(E, M_z)$ is proportional to the reciprocal of the adjusted $w(E, M_z)$.

As mentioned above, adjusting the weight for two-dimensional or multi-dimensional space requires massive calculation cost. To reduce the cost, for the MC sampling in the energy space, we use Boltzmann weight, i.e., $w(E, M_z) = w(M_z) \exp(-\beta E)$[39,40]. Then, the histogram of M_z space can be written as follows (using Eq. 14):

$$\begin{aligned} h(M_z) &= \sum_E h(E, M_z) \\ &= w(M_z) Z_{M_z}. \end{aligned} \tag{15}$$

Therefore, by obtaining a flat histogram in one dimensional space of M_z to adjust $w(M_z)$, the free energy can be calculated from Eq. 13:

$$\begin{aligned} F(\beta, M_z) &= -\beta^{-1} \ln \frac{C}{w_f(M_z)} \\ &= C + \beta^{-1} \ln w_f(M_z), \end{aligned} \tag{16}$$

where C is constant, w_f is the adjusted w when obtaining the flat histogram. Since the continuous spin system cannot determine C by calculation at each temperature, so in this study, we proceed with the calculation of the coercivity using the relative values of F. Although the above scheme requires the simulation for each temperature due to the use of Boltzmann weight, it significantly reduces the calculation cost for free energy as a function of M_z.

1/t algorithm

To obtain a flat histogram, the WLMC method adjusts the weight as $w(M_z') \to e^{-\eta} w(M_z')$ every update attempt (even if no update) of the spin state with a random walk, where $\eta(>0)$ is a modification factor, M_z' is the total magnetization of the state after the attempt. From the formulations of the previous section, update attempts of the spin state were performed according to the following transition probability:

$$\begin{aligned} P(E, M_z \to E'', M_z'') &= \min\left(1, \frac{w(E'', M_z'')}{w(E, M_z)}\right) \\ &= \min\left(1, e^{-\beta\left[E'' - E - G(M_z'') + G(M_z)\right]}\right), \\ G(M_z) &= \beta^{-1} \ln w(M_z), \end{aligned} \tag{17}$$

where E'' and M_z'' are the values of a trial state. Therefore, in the actual simulation, G is adjusted instead of w as $G(M_z') \to G(M_z') - \tilde{\eta}$, where $\tilde{\eta} = \beta^{-1}\eta$ (>0). This redefined modification factor $\tilde{\eta}$ has the unit of energy, which is convenient to adjust G with consistent values regardless of temperature.

Adjustment of G at every update attempt accelerates the convergence; however, it breaks a detailed balance condition. Thus, it is necessary to reduce $\tilde{\eta}$ so as not to affect the results of the MC simulation. To perform the reduction, the present study adopt the so-called 1/t algorithm[41] which resolves systematic error due to histogram flatness condition in the original WLMC method. The algorithm reduces the $\tilde{\eta}$ as $\alpha N_{bin}/t$, where α is proportionality coefficient (here, we set $\alpha = 1.0$ eV), t is the number of update attempts of the spin state and N_{bin} is the number of M_z levels in the simulation range of interest, $M_z \in [M_z^{min}, M_z^{max}]$. Note that, since the WLMC method requires to treat M_z discretely for the MC sampling with Eq. 17, in this study, we adopt the grid where $h(M_z)$ and $G(M_z)$ are discretized with the bins of $m_w = 0.3 - 0.5\mu_B$ width, and $N_{bin} = (M_z^{max} - M_z^{min})/m_w$. As a practical matter, during small t, the changes in $\tilde{\eta}$ is so large that the simulation does not convergence. Thus, the initial value of $\tilde{\eta}$ is set to be 1.0 eV, and it is reduced until $\tilde{\eta} \le N_{bin}/t$ (eV) as $\tilde{\eta} \to \tilde{\eta}/2$ at every random walker visit to the all the magnetization bins.

Algorithm 1.
The REWL method for M_z with 1/t algorithm.

```
Set spin model & parallelization

t = 0; h(:) = 0; G(:) = 0.0;  η̃ = 1.0; α = 1.0
for
    for  i-site=1:Ns
        Update i-site using Eq. (17)
        Calculate Mz
        t += 1
        h(Mz) += 1; G(Mz) -= η̃
    end
    Replica exchange using Eq. (18)
    t += 1
    h(Mz) += 1; G(Mz) -= η̃

    if ( min(h) > 0 for all processors )
        h(:) = 0;  η̃ /= 2
    end
    if ( η̃ < αNbin/t ): exit
end

for
    for i-site=1:Ns
        Update i-site using Eq. (17)
        Calculate Mz
        t += 1
        η̃ = αNbin/t
        h(Mz) += 1; G(Mz) -= η̃
    end
    Replica exchange using Eq. (18)
    t += 1
    η̃ = αNbin/t
    h(Mz) += 1; G(Mz) -= η̃

    Replica connection for G & h
    Check convergence, if ( true ): exit
end
Output G as free energy F
```

Replica exchange parallelization approach

For further large-scale simulation, we use the replica-exchange Wang–Landau (REWL) method[26,27], which is an efficient parallelization approach. The simple idea for parallelization in the WLMC method can be realized to divide the magnetization range by a small range and to allocate the piece into each processor. Each processor simulates the WLMC method individually. However, the small range may break ergodicity and inhibit the relaxation of the spin state. The REWL method is to recover the ergodicity by exchanging the spin configurations among these processors.

For the replica-exchange (RE), it is necessary to overlap the areas allocated to each processor, like Fig. 6. Previous research[27] proposed that the efficiently overlap ratio is 62.5–75% (we set 70%). In this study, every N_s spin update attempt, we try to exchange the spin configuration between neighbor processors according to the following exchange probability:

$$\begin{aligned} P_R(X \in n \leftrightarrow Y \in m) &= \min\left(1, \frac{w_n(Y) w_m(X)}{w_n(X) w_m(Y)}\right) \\ &= \min\left(1, e^{-\beta\left[G_n(X) + G_m(Y) - G_n(Y) - G_m(X)\right]}\right), \end{aligned} \tag{18}$$

where $n(, m)$ is the index of the adjacent processors, $X(, Y)$ is the spin configuration from which E and M_z can be calculated, and $w_n(, G_n)$ is the values of $w(, G)$ on the processor n. The exchange probability only depends on M_z and not on E. If the spin configurations are not in the overlapping range, $P_R = 0$.

As mentioned in Eq. 16, F (and G) can only be calculated as relative values. Thus, the values of F for the processors require to be corrected and connected so that the average value of the overlapping range is equal. After this connection, the average of F for all the processors is calculated as a result. Note that, just to improve connectivity among the processors, we

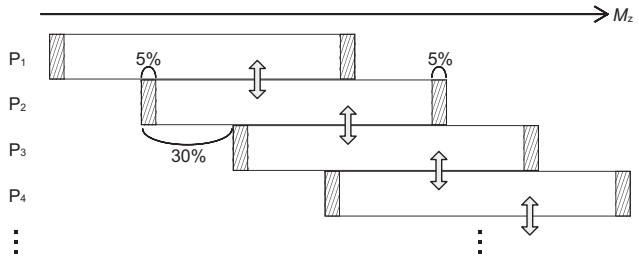

Fig. 6 Diagram of parallelization for the REWL method. The calculating range of the magnetization M_z is partitioned by many processors, here P_{1-4}. The double-headed arrows mean the replica-exchange and the shaded ranges denote the area to be omitted when connecting G among the processors (see text).

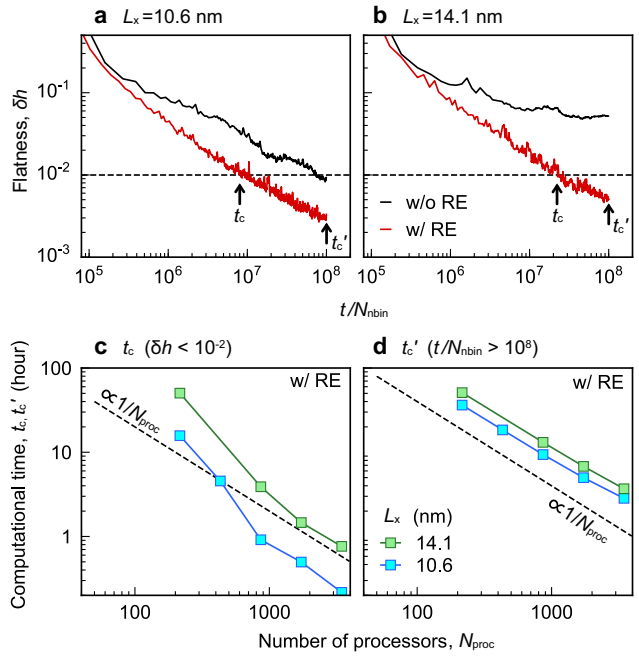

Fig. 7 Parallelization efficiency of replica exchange. The flatness δH as a function of $t/N_{bin}(= 1/\tilde{\eta}\,(1/\mathrm{eV}))$ at 0.46 T_C^{cal} of the $Nd_2Fe_{14}B$ spin model with the isolated grain for two sizes **a** $L_x = 10.6$ nm and **b** $L_x = 14.1$ nm. Black (Blue) lines are the results without (with) RE, which are performed by 864 processors. In the simulations, the calculated ranges of the magnetization are $M_z \in [-0.02M_z,\ 0.76M_z^t]$ for $L_x = 10.6$ nm and $M_z \in [0.3M_z^t,\ 0.76M_z^t]$ for $L_x = 14.1$ nm with $m_w = 0.5\mu_B$, where M_z^t is the maximum value of M_z in each spin system. **c** t_c and **d** t_c' are the computational times as a function of the number of processors N_{proc}, which satisfy the convergence conditions $\delta h < 10^{-2}$ and $t/N_{nbin} > 10^8$, respectively. Arrows in **a** and **b** denote the points corresponding to t_c and t_c'.

omit the edge ranges (5%, shown in Fig. 6) of each processor in the above correction and averaging (not so important).

To show the effectiveness of the RE, in Fig. 7a, b, we plot the flatness $\delta h = [\max(h) - \min(h)]/\mathrm{mean}(h)$ as a function of $t/N_{bin}(= 1/\tilde{\eta})$ in the simulations with and without RE. The accuracy of the REWL method is determined by the smallness of δH and $\tilde{\eta}$. Thus, the figure clearly indicates that RE is necessary to obtain a converged result, especially at large system size. The results in this study are set to satisfy the following convergence conditions: $\delta H < 10^{-2}$ and $\tilde{\eta} < 10^{-8}$ (eV). Figure 7c and d show the parallelization efficiency for the two system sizes in strong scaling with under the two convergence conditions. This result indicates that the parallelization is achieved with the ideal efficiency.

The pseudocode of the implemented methods in the present study is described in Algorithm 1. Through the methods, for large system size (up to 1,130,626 spins), we made it possible to calculate the free energy as a function of M_z.

DATA AVAILABILITY

The data reported in this paper is available from the corresponding author upon reasonable request.

CODE AVAILABILITY

The calculation codes used in this paper is available from the corresponding author upon reasonable request.

Received: 3 December 2019; Accepted: 10 April 2020;
Published online: 01 June 2020

REFERENCES

1. Gutfleisch, O. et al. Magnetic materials and devices for the 21st century: stronger, lighter, and more energy efficient. *Adv. Mater.* **23**, 821–842 (2011).
2. Chu, S. & Majumdar, A. Opportunities and challenges for a sustainable energy future. *Nature* **488**, 294–303 (2012).
3. Moriya, H., Tsuchiura, H. & Sakumav, A. First principles calculation of crystal field parameter near surfaces of $Nd_2Fe_{14}B$. *J. Appl. Phys.* **105**, 07A740 (2009).
4. Hrkac, G. et al. The role of local anisotropy profiles at grain boundaries on the coercivity of Nd2Fe14B magnets. *Appl. Phys. Lett.* **97**, 232511 (2010).
5. Mitsumata, C., Tsuchiura, H. & Sakuma, A. Model calculation of magnetization reversal process of hard magnet in $Nd_2Fe_{14}B$ system. *Appl. Phys. Express* **4**, 113002 (2011).
6. Suess, D. et al. Calculation of coercivity of magnetic nanostructures at finite temperatures. *Phys. Rev. B* **84**, 224421 (2011).
7. Hono, K. & Sepehri-Amin, H. Strategy for high-coercivity Nd-Fe-B magnets. *Scr. Mater.* **67**, 530–535 (2012).
8. Suzuki, M. et al. Magnetic domain evolution in Nd-Fe-B:Cu sintered magnet visualized by scanning hard X-ray microprobe. *Acta Mater.* **106**, 155–161 (2016).
9. Miyashita, S. et al. Perspectives of stochastic micromagnetism of Nd_2 Fe_{14} B and computation of thermally activated reversal process. *Scr. Mater.* **154**, 259–265 (2018).
10. Miyake, T. & Akai, H. Quantum theory of rare-earth magnets. *J. Phys. Soc. Jpn.* **87**, 041009 (2018).
11. Gaunt, P. Magnetic viscosity and thermal activation energy. *J. Appl. Phys.* **59**, 4129–4132 (1986).
12. Givord, D., Lienard, A., Tenaud, P. & Viadieu, T. Magnetic viscosity in Nd-Fe-B sintered magnets. *J. Magn. Magn. Mater.* **67**, L281–L285 (1987).
13. Givord, D., Lu, Q., Rossignol, M. F., Tenaud, P. & Viadieu, T. Experimental approach to coercivity analysis in hard magnetic materials. *J. Magn. Magn. Mater.* **83**, 183–188 (1990).
14. Okamoto, S. et al. Temperature-dependent magnetization reversal process and coercivity mechanism in Nd-Fe-B hot-deformed magnets. *J. Appl. Phys.* **118**, 223903 (2015).
15. Bance, S. et al. Thermal activation in permanent magnets. *JOM* **67**, 1350–1356 (2015).
16. Kronmüller, H., Durst, K. D. & Sagawa, M. Analysis of the magnetic hardening mechanism in RE-FeB permanent magnets. *J. Magn. Magn. Mater.* **74**, 291–302 (1988).
17. Givord, D., Rossignol, M. & Barthem, V. M. T. S. The physics of coercivity. *J. Magn. Magn. Mater.* **258-259**, 1–5 (2003).
18. Fischbacher, J. et al. On the limits of coercivity in permanent magnets. *Appl. Phys. Lett.* **111**, 072404 (2017).
19. Fischbacher, J. et al. Searching the weakest link: demagnetizing fields and magnetization reversal in permanent magnets. *Scr. Mater.* **154**, 253–258 (2018).
20. Toga, Y., Nishino, M., Miyashita, S., Miyake, T. & Sakuma, A. Anisotropy of exchange stiffness based on atomic-scale magnetic properties in the rare-earth permanent magnet Nd_2 Fe_{14} B. *Phys. Rev. B* **98**, 054418 (2018).
21. Gong, Q., Yi, M. & Xu, B.-X. Multiscale simulations toward calculating coercivity of Nd-Fe-B permanent magnets at high temperatures. *Phys. Rev. Mater.* **3**, 084406 (2019).
22. Zhang, L., Ren, W., Samanta, A. & Du, Q. Recent developments in computational modelling of nucleation in phase transformations. *NPJ Comput. Mater.* **2**, 16003 (2016).

23. Dittrich, R. et al. A path method for finding energy barriers and minimum energy paths in complex micromagnetic systems. *J. Magn. Magn. Mater.* **250**, 12–19 (2002).
24. Herbst, J. F. R2Fe14B materials: intrinsic properties and technological aspects. *Rev. Mod. Phys.* **63**, 819–898 (1991).
25. Toga, Y. et al. Monte Carlo analysis for finite-temperature magnetism of $Nd_2Fe_{14}B$ permanent magnet. *Phys. Rev. B* **94**, 219901–219901 (2016).
26. Nogawa, T., Ito, N. & Watanabe, H. Evaporation-condensation transition of the two-dimensional Potts model in the microcanonical ensemble. *Phys. Rev. E* **84**, 061107 (2011).
27. Vogel, T., Li, Y. W., Wüst, T. & Landau, D. P. Generic, hierarchical framework for massively parallel Wang-Landau sampling. *Phys. Rev. Lett.* **110**, 210603 (2013).
28. Wang, F. & Landau, D. P. Efficient, multiple-range random walk algorithm to calculate the density of states. *Phys. Rev. Lett.* **86**, 2050–2053 (2001).
29. Hirosawa, S. et al. The dependence of coercivity on anisotropy field in sintered R-Fe-B permanent magnets. *J. Magn. Magn. Mater.* **61**, 363–369 (1986).
30. Grönefeld, M. & Kronmüller, H. Calculation of strayfields near grain edges in permanent magnet material. *J. Magn. Magn. Mater.* **80**, 223–228 (1989).
31. Mohakud, S., Andraus, S., Nishino, M., Sakuma, A. & Miyashita, S. Temperature dependence of the threshold magnetic field for nucleation and domain wall propagation in an inhomogeneous structure with grain boundary. *Phys. Rev. B* **94**, 054430 (2016).
32. Vries, Jd., Bolhuis, T. & Abelmann, L. Temperature dependence of the energy barrier and switching field of sub-micron magnetic islands with perpendicular anisotropy. *N. J. Phys.* **19**, 093019 (2017).
33. Skomski, R., Zhou, J., Kirby, R. D. & Sellmyer, D. J. Micromagnetic energy barriers. *J. Appl. Phys.* **99**, 08B906 (2006).
34. Bance, S. et al. Grain-size dependent demagnetizing factors in permanent magnets. *J. Appl. Phys.* **116**, 233903 (2014).
35. Hinokihara, T., Nishino, M., Toga, Y. & Miyashita, S. Exploration of the effects of dipole-dipole interactions in Nd_2Fe_14B thin films based on a stochastic cutoff method with a novel efficient algorithm. *Phys. Rev. B* **97**, 104427 (2018).
36. Billington, D. et al. Unmasking the interior magnetic domain structure and evolution in Nd-Fe-B sintered magnets through high-field magnetic imaging of the fractured surface. *Phys. Rev. Mater.* **2**, 104413 (2018).
37. Nishino, M. et al. Atomistic-model study of temperature-dependent domain walls in the neodymium permanent magnet $Nd_2Fe_{14}B$. *Phys. Rev. B* **95**, 094429 (2017).
38. Nishino, M. & Miyashita, S. Nontrivial temperature dependence of ferromagnetic resonance frequency for spin reorientation transitions. *Phys. Rev. B* **100**, 020403 (2019).
39. Berg, B. A., Hansmann, U. & Neuhaus, T. Simulation of an ensemble with varying magnetic field: a numerical determination of the order-order interface tension in the $D=2$ Ising model. *Phys. Rev. B* **47**, 497–500 (1993).
40. Watanabe, K. & Sasaki, M. An efficient Monte-Carlo method for calculating free energy in long-range interacting systems. *J. Phys. Soc. Jpn* **80**, 093001 (2011).
41. Belardinelli, R. E. & Pereyra, V. D. Fast algorithm to calculate density of states. *Phys. Rev. E* **75**, 046701 (2007).

ACKNOWLEDGEMENTS

We acknowledge fruitful discussions with Satoshi Okamoto, Munetaka Sasaki, Masamichi Nishino, Taichi Hinokihara, and Satoshi Hirosawa. This work is partially supported by ESICMM, Grant Number JPMXP0112101004, through MEXT; by MEXT as a social and scientific priority issue (CDMSI) to be tackled by using a post-K computer. The computation was performed on Supercomputers at NIMS; ISSP, University of Tokyo; ACCMS, Kyoto University; RIIT, Kyushu University.

AUTHOR CONTRIBUTIONS

Y.T. and T.M. conceived and designed the basic research plan. A.S. proposed the plan from the viewpoint of the activation volume. Y.T. and S.M. discussed and developed the free-energy calculation approach for the coercivity. Y.T. performed the free energy and the coercivity calculation. Y.T., S.M., and T.M. wrote the paper. All authors discussed the results.

COMPETING INTERESTS

The authors declare no competing interests.

ADDITIONAL INFORMATION

Correspondence and requests for materials should be addressed to Y.T.

Reprints and permission information is available at http://www.nature.com/reprints

Publisher's note Springer Nature remains neutral with regard to jurisdictional claims in published maps and institutional affiliations.